An experimental study on the role of inter-particle friction in the shear-thinning behavior of non-Brownian suspensions

Muhammad Arshad, Abdelhamid Maali, Cyrille Claudet, Laurent Lobry, Francois Peters, Elisabeth Lemaire

Soft Matter

ARTICLE TYPE

Cite this: DOI: 00.0000/xxxxxxxxxx

An experimental study on the role of inter-particle friction in the shear-thinning behavior of non-Brownian suspensions†

Muhammad Arshad,[a] Abdelhamid Maali,[a] Cyrille Claudet,[b] Laurent Lobry,[b] Francois Peters,[b] and Elisabeth Lemaire,*[b]

Received Date
Accepted Date

DOI: 00.0000/xxxxxxxxxx

This paper focuses on shear-thinning in non-Brownian suspensions. In particular, it proposes a quantitative experimental validation of the model proposed by Lobry *et al. [J. Fluid Mech.*, 2019, **860**, 682-710] that links viscosity to microscopic friction between particles and, in particular, shear-thinning to load-dependent friction coefficient. To this aim, Atomic Force Microscopy (AFM) is used to measure the pairwise friction coefficient of polystyrene particles ($40\ \mu m$ in diameter), immersed in a Newtonian liquid, for different normal loads ranging from 10 to 1000 nN. It is shown that the inter-particle friction coefficient decreases with the load, contrarily to what is expected for macroscopic contacting bodies. The experimental friction law is then introduced into the viscosity model proposed by Lobry *et al.* and the results are compared to the viscosity of suspensions made of the same particles dispersed in the same liquid as those used for AFM measurements. The very good agreement between the measured viscosity values and those predicted by the model of Lobry *et al.* with the friction coefficient measured by AFM as input data shows the relevance of the scenario proposed by Lobry *et al.* and highlights the close links between the microscopic friction properties of the particles and the macroscopic rheological behavior of suspensions.

1 Introduction

The understanding and physical description of the rheology of concentrated suspensions has undergone important developments over the last 10 years, in particular by taking into account the frictional contacts between particles[1,2]. Several numerical[3–7], theoretical[8] and experimental[9–11] works have evidenced the marked influence of the inter-particle friction on the rheology of suspensions. In particular, friction is manifested by a strong increase of the suspension viscosity.

These studies resulted in a considerable progress in describing and interpreting the non-Newtonian behaviors manifested by concentrated non-Brownian suspensions. In particular, the scenario proposed by Seto *et al.*[12], Mari *et al.*[4] and Wyart & Cates[8] to explain the discontinuous shear-thickening (DST) observed in some highly concentrated non-Brownian suspensions turned out to be very valuable. This scenario is based on the existence of a transition from a flow regime where the particles do not come into direct contact (frictionless rheology) because the shear stress is not sufficient to allow the particles to counteract the repulsive interactions to a flow regime where the particles experience frictional contacts. This model has given rise to several experimental validations, including those of Guy *et al.*[13], Clavaud *et al.*[14], Comtet *et al.*[9] and Hsu *et al.*[15]. In the first two cases, the authors compare the rheological behavior of several suspensions whose DST characteristic stress is tuned either by varying the particle size[13] or the range of the repulsive force between particles[14]. Comtet *et al.*[9] present a direct measurement of the inter-particle friction by atomic force microscopy which reveals two regimes: for small loads, the contact is lubricated whereas, beyond a critical normal force, the contact appears to become frictional. The authors establish a quantitative relationship between this critical load and the stress associated with DST. At last, Hsu *et al.*[15] combines the tuning of the DST transition by varying the roughness of the particles and measurements of inter-particle friction coefficient by AFM, using an accurate method they had previously developed[16]. Their results illustrate in an extremely clear way the strong links between the rheology of suspensions and tribological properties of the particles. Another recent paper[17] that combines AFM and rheometric measurements shows how adhesion modifies the DST transition.

The shear-thinning behavior exhibited by most non-Brownian suspensions has been less studied but it has been often reported in the literature[18–23]. In colloidal suspensions, when adhesive

[a] *Laboratoire Onde et Matière d'Aquitaine, UMR 5798 CNRS-Université Bordeaux, 33405 Talence cedex, France*
[b] *Institut de Physique de Nice, UMR 7010 CNRS-Université Côte d'Azur, 06108 Nice cedex 2, France; E-mail: elemaire@unice.fr.*

forces are present between particles, shear-thinning can be explained by a competition between the adhesive forces under the effect of which the particles tend to form flocs and the hydrodynamic forces which break these aggregates. These attractive colloidal forces are known to be active in Brownian suspensions but their effects in non-Brownian suspensions have been little studied. It is only recently that Richards *et al.*[23] used the constraint-based rheology model previously proposed by Guy *et al.*[13] to analyze yielding in adhesive and frictional non-Brownian suspensions. The authors stress the differences between this class of materials where adhesion acts as a rolling constraint between contacting particles (sticky contacts) and attractive Brownian suspensions where particles are subject to attractive interaction without contacting. Papadopoulou *et al.*[22] showed, by using non-Brownian silica particles with different morphologies, surface functional groups and suspending media that shear-thinning can originate either from adhesion forces between particles or from load-dependent interparticle friction. This last scenario was first evidenced by Chatté *et al.*[10] who proved that the shear-thinning which takes place for higher stresses than the DST characteristic stress was correlated to the decrease of the friction coefficient of the particles as the contact force between particles increases. The authors used a quartz-tuning fork based atomic force microscope to measure the friction coefficient of two types of PVC particles immersed in a plasticizer, as a function of normal load. They also measured the viscosity of suspensions made of both types of particles and showed that there was a very strong correlation between the value of the jamming fraction (extrapolated from the viscosity measurement at a given volume fraction) and the value of the friction coefficient measured by the AFM. This was the first experimental proof that shear-thinning and friction could be related. Around the same time, Tanner *et al.*[24] proposed a model based on a bootstrap mechanism of friction where the friction coefficient is a decreasing function of the sliding speed between particles and Lobry *et al.*[25] showed that it was possible to quantitatively capture the shear-thinning by properly modeling the contact between particles. This model is based on the assumption that, in a shear flow, the particles come into contact via one or a few asperities. This idea that the contact between particles is promoted by surface asperities is now widely accepted. It has been particularly confirmed by experimental observations which evidenced the signature of such contacting asperities on particle pair trajectories[26] and pair distribution functions[27] in sheared suspensions. As a consequence, in the frame of a contact through one or a few asperities, it is expected that the friction coefficient will no longer be constant, in contrast to what happens for macroscopic contact involving many asperities[28]. In this model, roughnesses are represented by hemispheres whose radius is of the order of one thousandth of the radius of the particles. This roughness height is standard for polymer particles of a few tens of microns[29,30]. More and Ardekani[31] used the model proposed by Lobry *et al.* to study the influence of roughness size on the viscosity of a suspension. These two numerical studies use the single-contact friction model proposed by Brizmer *et al.*[32] where the contact between a plane and a perfectly smooth sphere (mimicking an asperity) is considered. Two regimes are identified: for small loads F_n, the contact is assumed to be elastic and can then be modeled by the Hertz contact theory where the contact area varies as $F_n^{2/3}$. The friction coefficient which is given by the ratio between the tangential force that is proportional to the contact area and the normal force thus varies as the normal force to the power -1/3. For higher loads, the contact enters the plastic regime and the friction coefficient levels off at a constant value. The transition from the elastic regime to the plastic regime occurs at a given value of the normal load, L_c, which depends on the radius of the asperities and on the material characteristics of the particles (Young modulus, yield strength and Poisson's ratio). As a consequence, this microscopic friction model introduces of a stress scale into the rheology of suspensions and thus opens up the possibility that the viscosity depends on the applied stress.

Finally, since the contact force experienced by the particles is related to the shear stress σ and the particle radius a through $F_n \sim 6\pi a^2\sigma$, the elastic-plastic contact law results in two marked rheological behaviors, from shear-thinning at low stress, where the mean friction coefficient decreases, to Newtonian at high stress , where the friction coefficient levels off. Lobry *et al.* also proposed a correlation law, based on their simulation data, allowing to compute the whole viscosity curve from the microscopic friction law alone, making it possible to account for any particular friction law. In this model, the relevant interparticle force intensity that controls the mean interparticle friction coefficient is simply $F_n = 6\pi a^2\sigma/1.69$ where the scaling factor 1.69 is introduced for the model to fit with the earlier constant friction coefficient simulations of Gallier *et al.*[3].

The aim of this paper is to present a quantitative experimental validation of the model proposed by Lobry *et al.*[25], hereafter called *STIVF* model (for Shear-Thinning Induced by Variable Friction model), that links viscosity to friction and, in particular, shear-thinning to load-dependent friction coefficient. For this purpose we have measured by using an AFM the pairwise friction coefficient of polystyrene particles, immersed in a Newtonian liquid, for different normal loads. The friction coefficient obtained is then introduced into the *STIVF* model. The viscosity of suspensions made of the same particles dispersed in the same liquid as the ones used for AFM measurements is then measured for several particle volume fractions. The very good agreement between the measured viscosity values and those predicted by the *STIVF* model with the friction coefficient measured by AFM as input data shows unambiguously the relevance of the scenario proposed by Lobry *et al.*.

In section 2, we present the rheological measurements. The AFM measurement are described in Section 3 while section 4 is devoted to the comparison of the experimental results with the viscosity model that includes a load-dependent friction coefficient between particles.

2 Viscosimetric measurements

2.1 Materials

The suspensions are made of polystyrene particles (*Dynoseeds TS40 from Microbeads*) suspended in a mixture of water(90 *vol%*), Ucon oil (*75-H-90,000, Dow*) and a 1.5% aqueous solution of Zinc

Bromide. Ucon oil is added to water to increase the viscosity of the suspending fluid in order to be able to perform rheology measurements over a wide range of shear stresses and still have a low Reynolds number. Zinc Bromide is added to precisely match the density of the liquid to that of the particles, which has been measured to be $1045 \pm 4\ kg/m^3$. The viscosity has been measured for various stresses comprised between 0.1 and 100 Pa. In this range, the suspending liquid is Newtonian with a viscosity equal to $0.055 \pm 0.002\ Pa.s$ at $T = 25^oC$. The nominal diameter of the particles is 40 μm. They are supposed to be monodisperse but Dai *et al.*[33] determined precisely the size distribution of the same kind of particles and showed a slight polydispersity with a standard deviation in size of about 4.3 μm around a mean diameter of $2a = 40.3\ \mu m$. By AFM imaging, we characterized the roughness of the particles that has been found to be around 36 nm (RMS value)[25].

We studied the variation of viscosity with shear stress for five particle volume fractions, ϕ: 0.405, 0.45, 0.47, 0.49 and 0.507 and we compare the behavior of suspensions whose particles have been previously washed (WP) or not (RP). WP particles are washed by several steps (≈ 5) of filtration and redispersion in deionized water after which they are dried in a vacuum oven during 12 hrs at $T = 60^oC$. Dynoseeds TS 40 (*MICROBEADS*) particles are manufactured by using a technique of aqueous dispersion polymerisation that involves the presence of a stabilizer in the dispersion[34]. Thus, by washing the particles, we anticipate that the colloidal interactions between particles will be modified. The role of colloidal forces in suspension rheology has been much less studied for non-Brownian suspensions than for Brownian suspensions, probably because it is much weaker. However, recent studies have shown that changing the physico-chemical properties of non-Brownian suspensions has a noticeable impact on rheology[14,22,23].

2.2 Rheometric experiments

The viscosity has been measured in rotating parallel plate geometry. The radius of the disks, R, is 30 mm and the gap height is set to 1.2 mm, *i.e.* 30 particle diameters, so that wall ordering effects can be neglected[35]. Rotating plate geometry provides the advantage that no migration[36] or very slow migration[37] takes place. The inconvenience of using such a geometry to study non-Newtonian materials is obviously the variation of the shear rate with radial position. To account for shear rate variation from 0 at the center to $\dot{\gamma}_R = \Omega R/h$ at the rim (Ω being the angular velocity of the rotating plate), the Mooney-Rabinovitch correction is used to correct the shear stress:

$$\sigma_R = \frac{\sigma_{rheo}}{4}\left(3 + \frac{d\,ln\,\sigma_{rheo}}{d\,ln\,\dot{\gamma}_R}\right) \quad (1)$$

where $\sigma_{rheo} = 2\Gamma/\pi R^3$ with Γ the torque applied by the rheometer.

The viscosity is then obtained :

$$\eta = \frac{\sigma_R}{\dot{\gamma}_R} \quad (2)$$

Viscosity is measured by imposing stress steps whose duration varies depending on the intensity of the stress. Indeed, the steady viscosity of a suspension is only reached when its microstructure is at equilibrium, which requires that the suspension has been sheared over a deformation of several units. In the following, we will use the normalized viscosity defined by the ratio of the suspension viscosity to the suspending fluid viscosity: $\eta_S = \eta/\eta_0$. The variation of η_S with particle volume fraction is shown in Fig.1. In this figure, two different behaviors can be observed, depending on whether the particles have been washed (WP) before the suspension was made, or if raw particles (RP) where used. As said before, washed particle suspensions are likely to be less stable than non-washed suspensions since washing the particles removes all or part of the surfactant. The particles are then possibly subject to adhesive forces. An order of magnitude of these forces can be obtained by using the JKR theory[38]:

$$F_{adh} = \frac{3}{2}\pi w r_c \quad (3)$$

where w is the energy per contact area. Following Hodges *et al.*[39], for r_c, we take the curvature radius of an asperity which is of the order of a hundred nanometers[25,40,41]. The value of w is found in the literature[42,43] and is of the order of 60 to 80 mJ/m^2. These values lead to $F_{adh} \approx 30\ nN$ which corresponds to a typical shear stress of $\sigma_{adh} = F/6\pi a^2 \approx 4\ Pa$. This order of magnitude is consistent with what is observed in Fig. 1 where the viscosity values of the two types of suspensions are shown to be different for stresses typically lower than 5 Pa. In this low stress range ($\sigma < 5Pa$), the viscosity of the WP suspensions increases sharply as the shear stress decreases, regardless of the volume fraction value. On the contrary, the viscosity of the less concentrated RP suspensions (i.e. $\phi = 0.405,\ 0.45$ and 0.47) tends towards a plateau as the shear stress decreases. Even a relatively low but still visible shear-thickening regime can be observed for stresses below typically 1 Pa. The explanation for this shear-thickening is presumably the same as that proposed by Seto *et al.*[12] to explain DST: the observed continuous shear-thickening should originate from a competition between the repulsive forces resulting from the presence of the surfactant which tends to prevent contact between particles and the forces associated with the flow which, on the contrary, promote frictional contacts between particles. The characteristic shear stress for which shear-thickening takes place is smaller than the one usually reported in studies dedicated to shear-thickening. However, one must keep in mind that the particles used in the present study are as large as $40\,\mu m$ in diameter. Guy *et al.*[13] have shown, based on their own data and using the data collected by Barnes in his review[44], that the critical shear-thickening stress varies as a^{-2}. The values of critical stresses reported by these authors for particles of several tens of microns in size are of the order of $0.1\,Pa$ which is consistent with the findings of Fig. 1. As a last argument supporting that the flow regime is that of a suspension in the thickened state, we would like to stress that the relative viscosity values that we measure above $\sigma \approx 1\,Pa$ are consistent with those that are measured –or calculated numerically– indifferently in concentrated non-Brownian frictional suspensions[3,7,21,25] or in shear-thickening suspensions beyond the shear-thickening transition[4,13,45]. Finally, note that

for the two highest particle volume fraction, no peak viscosity is observed anymore in Fig. 1 for the raw particle suspensions. This finding is consistent with the recent work of Singh *et al.*[46] who studied how shear-thickening transition can be obscured by the presence of adhesive forces. On the one hand, the onset stress of shear-thickening does not vary with particle volume fraction[1,4,13] while, on the other hand, the yield stress increases with increasing particle volume fraction[22,23]. It is therefore likely that the residual adhesion forces cause a yield stress whose value increases with increasing ϕ and which, for large enough volume fractions, conceals the shear-thickening transition.

Above 5 *Pa*, both suspensions behave the same. This means in particular that the shear-thinning behavior in the range of stresses above 5 Pa cannot be attributed to adhesive properties of the particles. This suggests, as proposed by Papadopoulou *et al.*[22], that shear-thinning may originate from several mechanisms, including adhesion or friction. In the following, we will show how the shear-thinning observed for shear stresses larger than a few Pa –which is almost the same for the two types of suspensions– can be explained by a load-dependent inter-particle friction as proposed by Lobry *et al.*[25] in the *STIVF* model. To this aim, we first measure the frictional properties of the TS40 polystyrene particles immersed in the mixture ($water + Ucon\ oil + ZnBr$). This will be described in the next section.

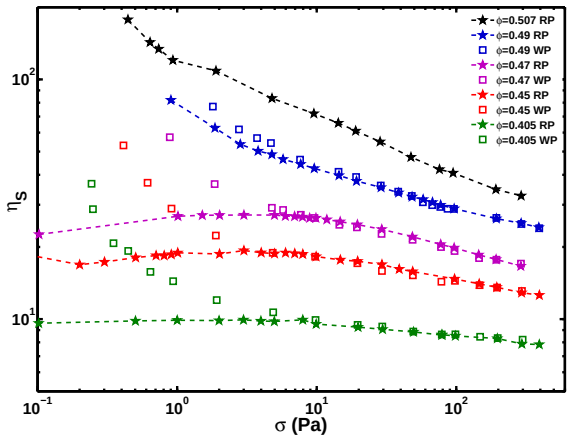

Fig. 1 Variation of the viscosity with shear stress for suspensions made of either washed (hollow squares) or non-washed (stars) TS40 particles.

3 AFM measurements

The experiment was performed using Atomic Force Microscope AFM (Bioscope, Bruker). The system is equipped with a liquid cell (DTFML-DD-HE, Bruker) that allows dynamic mode working in liquid environment. A Dynoseed TS40 sphere of radius 20 μm is attached to the end of an AFM rectangular cantilever (NSG-11/tipless, *TipsNano*, length 130 μm, width 35 ± 3 μm and thickness 2 ± 0.5 μm) using epoxy glue (*Araldite*)(see Fig. 2.a). Other particles are deposited on a glass substrate coated with a thin layer of glue and a jet of filtered air is used to remove particles that were not stuck on the surface. The particle-seeded substrate is mounted on a 3-axis piezoelectric actuation stage (*NanoT series, Mad City Labs*) that allows lateral displacement (along y-axis) of

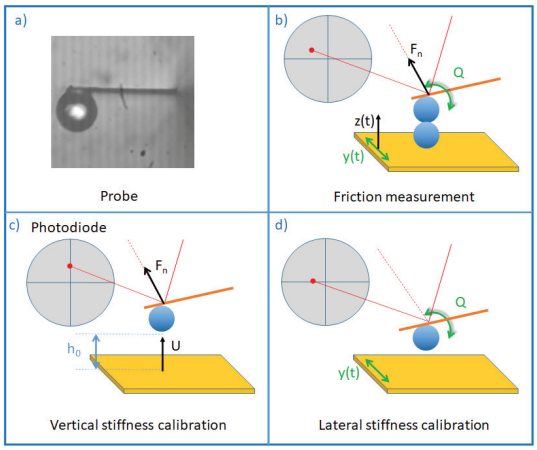

Fig. 2 AFM measurement device. a) microsphere glued on a rectangular cantilever. b) sketch of friction measurement. c) and d) sketches of vertical and lateral stiffness calibrations.

up to $20 \mu m/V$, and vertical displacement (along z-axis) of up to 5 $\mu m/V$ under closed loop control (Fig. 2.b). After centering the colloidal probe with one of the spheres on substrate, we simultaneously measured the vertical and lateral forces. Both vertical and lateral deflections of the cantilever are measured by a laser beam that is reflected on the back surface of the cantilever and detected by a four segments photodiode. The measured photodiode signals are recorded with an Analog to Digital (A/D) acquisition board (*PCI-4462, Nat. Instr. USA*) with a sampling rate of 2kHz.

3.1 Calibration

Since the vertical and lateral force are deduced from the photodiode signal, it is necessary to determine the conversion factors, k_n and k_y that enable to convert the photodiode output voltage into force values:

$$\begin{aligned} F_n &= k_n V_z \\ F_t &= Q/2a = k_l V_y/2a = k_y V_y \end{aligned} \tag{4}$$

where F_n and Q are the normal force and the torque applied to the cantilever. V_z and V_y are the output signals of the photodiode and F_t is the tangential frictional force.

Many calibration methods exist (Cleveland method[47], Sader method[48], thermal noise method[49], hydrodynamic method[50]) and among them we chose the hydrodynamic method. To determine k_n, we followed Craig and Neto[50] and calibrated the vertical stiffness of the cantilever by measuring the hydrodynamic drag on the sphere attached to the cantilever while a flat stiff substrate is approaching at constant velocity, U (Fig. 2.c). For a perfectly smooth sphere, in the lubrication approximation (i.e. $h_0 << a$), a linear relationship between the normal force, F_n, and the inverse of the separation distance, h_0, is expected:

$$F_n = k_n V_z = 6\pi\eta a^2 \frac{U}{h_0} \tag{5}$$

To account for probe roughness, Eqn. (5) is modified by adding to the separation distance a constant, h_c, which is related to rough-

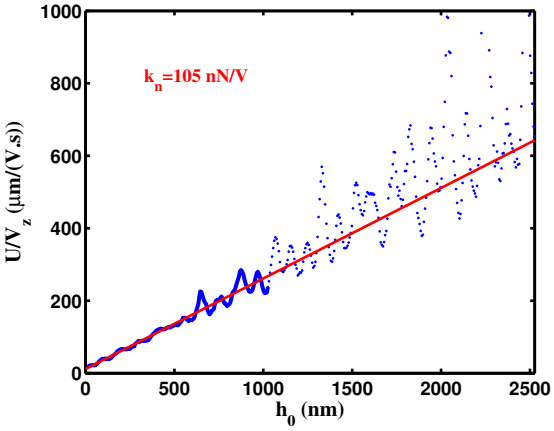

Fig. 3 Ratio of the approaching velocity ($U = 39\,\mu m/s$) to the output signal of the photodiode corresponding to the vertical deflection as a function of tip-substrate separation. For this calibration the probe is immersed in a mixture of water and glycerol with a viscosity of $0.050\ Pa.s$. The conversion factor, k_n is obtained by fitting the data in the linear region (dark blue line) with the lubrication equation (Eqn. (6)): $U/V_z = k_n(h_0+h_c)/(6\pi\eta a^2)$ where h_c is a constant free parameter that accounts for probe roughness and for possible error on the determination of the zero of separation. From the fitting of the experimental data, we obtain $k_n = 105 \pm 5 nN/V$ and $h_c = 37\,nm$.

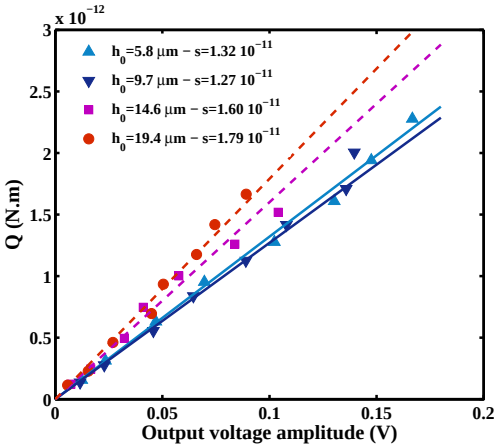

Fig. 4 Hydrodynamic calibration of the lateral stiffness. The probe is immersed in a mixture of water and glycerol with a viscosity of $0.049 Pa.s$ and the substrate is oscillated at a frequency of $120\ Hz$ while the probe is at a distance h_0. The torque calculated from Eqns. (7,8) and (9) is plotted against the amplitude of the photodiode output voltage for four different values of h_0. The slope of the lines (s) varies with h_0 but tends towards a constant value when h_0 becomes sufficiently small. The value of the slope obtained for the two smallest separation distances is used to determine the lateral conversion factor: $k_l = 1.30\ 10^{-11}\ N.m/V$.

ness morphology (density, extension, height...)[51]:

$$F_n = k_n V_z = 6\pi\eta a^2 \frac{U}{h_0 + h_c} \tag{6}$$

In addition, inferring the exact position of the zero of separation raises important difficulties. So, for these two reasons, we estimated that it was appropriate to consider h_c as a free parameter. Fig. 3 shows the variation of the approaching velocity divided by the photodiode signal as a function of the tip-substrate separation (see Supplementary Materials, for other calibration curves obtained with an other value of the approaching velocity and with a withdrawing velocity and details on the analysis). A linear variation of $1/V_z$ versus (h_0+h_c) is observed and a linear fitting provides a measurement of k_n (see Eqn 6). The fitting is performed for separation distances lower than typically $1000\ nm$ (region marked by the continuous curve in Fig. 3) and provides $k_n = 105\,nN/m$. For higher separation distances, the scatter of the data is rather important but extending the fitting range hardly modifies the fitting results. The uncertainty on the value of k_n is dominated by the uncertainty in the viscosity value which is estimated to 5%. Thus we obtain $k_n = 105 \pm 5\ nN/V$. For the constant h_c, we obtained $37\,nm$ which is also the order of magnitude of the roughness height on the probe surface. Note that, for any purpose, we also calibrated the photodiode sensitivity (i.e. the conversion factor between the photodiode output voltage and the cantilever deflection, C_n) with a force curve on a stiff substrate and obtained $C_n = 0.037\ V/nm$ which gives a spring constant $K_{spring} = 3.9 \pm 0.1\ N/m$.

To calibrate the lateral stiffness, we used the method proposed by Ryu and Franck[52]: the substrate is positioned at a given position, h_0 to the colloid probe and is oscillated horizontally: $y_s = y_0 \cos\omega t$ (Fig. 2.d). The horizontal motion of the substrate gives rise to a Couette flow between the flat and the particle which is subjected to both a viscous drag force and a torque that are given by:

$$\begin{aligned} F_{visc} &= 6\pi\eta a U f^* \\ \tau_{visc} &= 8\pi\eta a^2 U \tau^* \end{aligned} \tag{7}$$

where f^* and τ^* are functions of h_0/a. To compute f^* and τ^*, we use the asymptotic formulas given by Goldman *et al.*[53]:

$$\begin{aligned} f^* &= -\frac{8}{15} ln\left(\frac{h_0}{a}\right) + 0.9588 \\ \tau^* &= \frac{1}{10} ln\left(\frac{h_0}{a}\right) + 0.1895 \end{aligned} \tag{8}$$

Assuming that the torque applied on the cantilever itself is negligible, the total torque exerted on the ensemble (cantilever + micro-particle) can be written as:

$$Q = F_{visc} a + \tau_{visc} \tag{9}$$

Fig. 4 shows the relation between the torque amplitude calculated with Eqns. (7, 8) and (9) where $U = y_0\omega$ and the amplitude of the photodiode output voltage, V_{y0}. It is observed that V_{y0} increases linearly with Q and k_l is given by the slope. The slope varies with h_0 which was expected since the expressions of the force and the torque as a function of the separation distance between the particle and the plane taken from[53] are valid only for small separation distances. Furthermore, we neglected the effect of the cantilever itself which is likely to modify the flow around the colloid probe. The relative contribution of this effect on Q becomes smaller as the separation distance decreases. For these

two reasons, the calibration accuracy increases as h_0 decreases. But, on the other hand, the determination of the distance h_0 is quite tricky. Therefore, reducing this distance to too low values is likely to introduce an important error in the evaluation of the torque. $h_0 \approx 6\ \mu m$ appeared to be a good compromise value and we found $k_l = 1.30\ 10^{-11}\ N.m/V$.

3.2 Friction measurements

To measure the friction force between TS40 particles, the flat substrate is replaced by the particle-seeded substrate whose horizontal position is controlled so as to vertically align one of the particles of the substrate with the particle attached to the cantilever. Then the substrate is vibrated in the y-direction with variable amplitudes ($\sim 1\ \mu m$) and frequencies between 25 and 100 Hz. It is simultaneously moved vertically at constant speed ($\sim 0.1 \mu m/s$). An example of force displacement curve is presented in Fig. 5. The

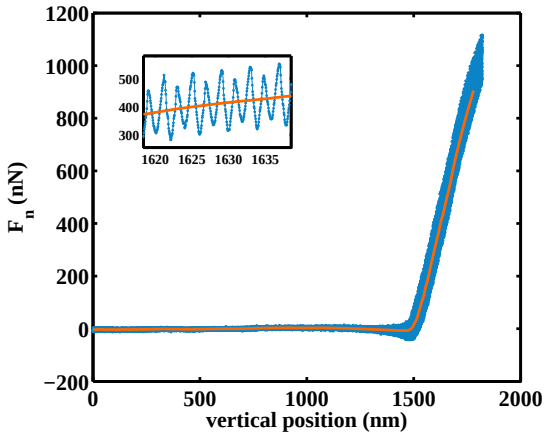

Fig. 5 Normal force as a function of the vertical position of the substrate. The blue curve is the measured force while the orange line is the value of the force averaged over a period of oscillation of the substrate. Insert: zoom of the variation of the normal load with vertical position.

normal force is the combination of a continuous component that increases as soon as the particles touch (the vertical velocity of the substrate is sufficiently small for the vertical lubricating force to be negligible) and an oscillating force whose period is that of the horizontal vibration of the substrate (see insert of Fig. 5): $F_n(t) = F_n^{mean}(t) + F_n^{osc} cos\omega t$. The quasi-periodic component of F_n comes from geometry and is caused by the curvature of the particles. Fernandez *et al.* [16] studied in detail the effect of particle curvature on the AFM measurement of normal and tangential forces and showed that it could be very important if the particle size is not very large compared to the oscillation amplitude of the substrate. But, it is not the case in our study where the particles have a radius of 20 μm while the vibration amplitude of the substrate is of the order of one micron, which implies that, during a cycle, the height of the particle probe varies by about $\delta h \approx 25\,nm$ to remain in contact with the particle stuck on the substrate, which corresponds to very small angles $\sqrt{2\delta h/a}$. In particular, this evaluation is fully compatible with the amplitude of oscillation of the normal force ($F_n^{osc} \approx K_{spring}\,\delta h \approx 100\,nN$). We can get rid of curvature effects by considering only the measurements of normal force and tangential force over a sufficiently small interval of y so that the variation of the normal force is small in comparison with its mean value. To this aim, for each quasi-cycle $(y,\ F_n)$, we consider only the central region whose extension is chosen so that the normal force varies by less than 10% (see blue squares in Fig. 6). In this region, the friction coefficient is defined by

$$\mu = \frac{< F_t^{up} > - < F_t^{down} >}{2\ F_n^{mean}} \tag{10}$$

where F_t^{up} and F_t^{down} are the tangential forces recorded when the substrate moves to the right ($y' > 0$) or to the left ($y' < 0$) and the symbol $< ... >$ denotes the average over the chosen interval of y. This is illustrated in Fig. 6 where the typical variations of the normal force and tangential force during a cycle are shown.

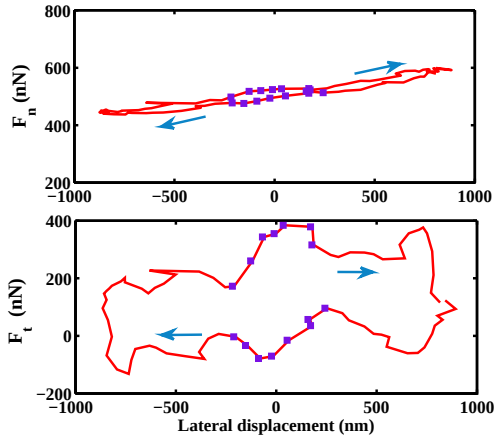

Fig. 6 Variation of the normal (up) and tangential (down) force versus the lateral position of the substrate during one period of oscillation. During a cycle, both the normal force and the absolute value of the tangential force vary. Therefore, to calculate the coefficient, we only select the data for which the normal force deviates from its mean value by lower than 10% (blue squares).

The friction coefficient is measured for six different particle pairs, for three different frequencies (25, 50 and 100) and different lateral displacement amplitudes (comprised between 600 and 2000 nm). Fig. 7 shows the measured friction coefficient for 12 realizations (small symbols) and the averaged friction coefficient (solid line). It should first be noted that, as expected in the frame of a mono-contact model, the friction coefficient decreases as the normal load increases. Secondly, the measured coefficients of friction vary quite significantly from one realization to another. These differences are not due to experimental uncertainties, but rather to a spatial variation of the local friction coefficient which is expected, especially taking into account the surface roughness. We recall that the characteristic extension of the surface roughness is of the order or slightly less than one micron, which is also the order of magnitude of the lateral displacement on which the friction is probed. It is therefore not surprising that, from one realization to another, the local friction coefficient changes. On the contrary, we verified that neither the frequency nor the amplitude of vibration of the substrate affected the measurement of the friction coefficient.

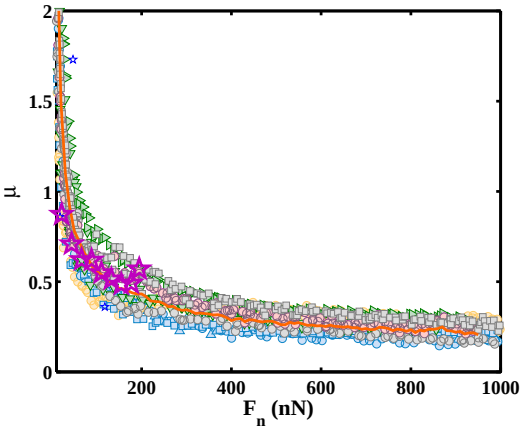

Fig. 7 The measured friction coefficient for six different particle pairs, different frequencies (25, 50 and 100 Hz) and different lateral displacement amplitudes (ranging from 600 to 2000nm) is depicted against the normal force. The pink stars correspond to quasi-static measurements (frequency $1\,Hz$, amplitude $1500\,nm$). The orange line is the mean friction coefficient averaged over all the realizations.

In Fig.7, some results obtained in quasi-static mode are also represented (large pink stars). These measurements were performed using a cantilever ten times softer (vertical stiffness $0.364\ N/m$) and vibrating the substrate at low frequency ($1\ Hz$) with an amplitude of $1.5\mu m$. The values of the quasistatic friction coefficients and their evolution with the load are comparable to what is obtained in dynamic mode. However, these quasistatic measurements can hardly lead to reliable quantitative results because they require a rather long duration of experiment during which the normal force is likely to vary due to the drift in time of the photodiode response. This issue may probably explain why the friction coefficient measured for the largest of the applied normal force –and which in the experiment was the last measurement– deviates from the general trend of the variation of μ with F_n (see Fig.7). Furthermore, as seen before, the friction coefficient measured for such small contact forces is essentially a statistical quantity since the result of the measurement depends on the local geometry of the asperities at contact. Therefore, in order to obtain a reliable average μ value, a large number of measurements are necessary. For these reasons, we decided to use the measurements made in quasistatic mode only to validate the dynamic measurements.

Fig.7 shows unambiguously that the inter-particle friction coefficient decreases with the load, contrarily to what is expected for macroscopic bodies whose friction is determined by a constant friction coefficient. Such a load-dependent friction coefficient has been described by Brizmer *et al.* [32] who considered the contact between a perfectly smooth sphere and a flat. The resulting friction coefficient is given by:

$$\mu = 0.27\ coth\left(0.27\left(\frac{F_n}{L_c}\right)^{0.35}\right) \tag{11}$$

This expression accounts for the transition from elastic deformation of the sphere ($L < L_c$) to plastic deformation ($L > L_c$). In the elastic deformation regime, the Hertz contact law is approximately recovered. In this regime, the contact area varies as $F_n^{2/3}$ and, since the tangential force is proportional to the contact area, the friction coefficient decreases as $F_n^{-1/3}$. Eqn. (11) leads to $\mu \propto F_n^{-0.35}$ in this regime, which is consistent. In the plastic regime, the friction coefficient levels off at the value 0.27. L_c is a function of the Young modulus, Poisson ratio and Yield stress of the material, and of the contacting sphere radius as well [32]. Coming back to the case of the microspheres whose friction coefficient is measured here, it is likely that, given the magnitude of the normal forces involved in the AFM experiment, the particles come into contact through only one or a few asperities present on their surface [§]. These correspond to the smooth sphere of the model of Brizmer *et al.*, which consequently predicts a decrease in the friction coefficient with the load.

The friction coefficient computed from Eqn. (11) is displayed in Fig. 8, together with the mean friction coefficient from the experiments (symbols). At very small normal load, our results are in fairly good agreement with Brizmer's predictions but then Brizmer model predicts a slower decrease in the friction coefficient than the one we have measured. Also note the discrepancy between the experimentally measured μ values and those predicted by Brizmer *et al.* for high values of F_n. However, these differences are not surprising since Eqn. (11) considers an idealized contact between a plane and a hemisphere whereas, in our case, the roughness geometry is probably more complicated. There is therefore no reason why the friction law should strictly obey Brizmer model. Finally, an equation close to that proposed by Brizmer *et al.* is fitted to the measured mean friction coefficient (see orange line in Fig.8). The friction coefficient at infinite normal load is taken as 0.18 and L_c and n are free parameters:

$$\mu = 0.18\ coth\left(0.18\left(\frac{F_n}{L_c}\right)^{n}\right) \tag{12}$$

It is recalled here that L_c is to be considered as the critical load that marks the transition from the elastic deformation of one asperity at low load to the plastic deformation at higher load. The best fit (in the range $F_n \in [10, 950\ nN]$) is obtained for $L_c = 33.2\ nN$ and $n = 0.54$. The value of L_c is quite close to that estimated by Lobry *et al.* [25] on the basis of the material properties of the particles ($L_c = 20nN$) but, as said before, we measured a faster decay of the friction coefficient with load than that predicted by Brizmer *et al.* ($n = 0.54$ in our measurement while $n = 0.35$ in Brizmer model).

§ The relevance of considering a single asperity contact is extensively discussed in [25] but a quick argument can be provided by evaluating the roughness deformation due to contact. According to Hertz theory, the typical deformation of an asperity is given by: $\bar{\delta} = \left(F_n/\left(0.75E^*\sqrt{r_c}\right)\right)^{2/3}$ where $r_c \approx 100\,nm$ is the radius of curvature of an asperity and $E^* = E/(1-\nu^2)$ with $E \approx 3\,GPa$, the Young modulus of polystyrene and $\nu \approx 0.4$, the Poisson's ratio. Taking for F_n the maximum force involved in the present study: $F_n \approx 1\,\mu N$, we obtain $\bar{\delta} \approx 10\,nm$. Thus the typical asperity indentation is much smaller than the roughness height which justifies that the contact between particles involves only one or a few asperities.

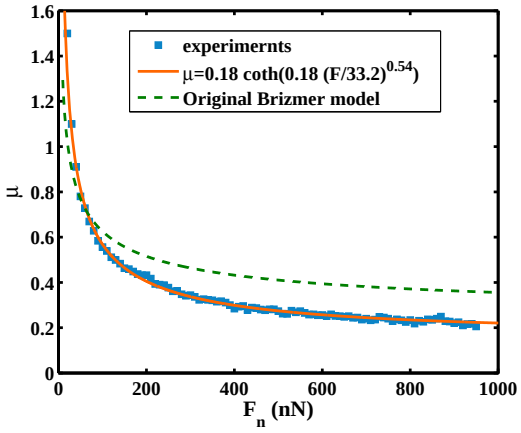

Fig. 8 Variation of the friction coefficient with normal load. The blue squares correspond to the average of all the measurements shown in Fig. 7 and obtained for different particle pairs, amplitudes and frequencies. The orange line is the result of the data fitting with Eqn. (12) which gives the following fitting parameters: $L_c = 33.2\ nN$ and $n = 0.54$. For the sake of comparison the original result of Brizmer *et al.*[32] is also shown (dashed green line).

4 Viscosity deduced from friction

In this section, we will test the scenario used in the *STIVF* model to explain the shear-thinning observed in non-Brownian suspensions by a friction coefficient that varies with load. Let us first recall the main features and results of the model. The authors performed discrete simulations of sheared suspensions, where the friction coefficient between particles obeys Eqn. (11). Suspensions are bidisperse (with particle radii a_1 and $a_2 = 1.4a_1$ in equal number) in order to avoid cristallization. They found that the variation of the computed viscosity with shear rate could be accurately described using a very simple and physically sound model. The main idea is that the overall shear stress controls the normal force between particles, hence the relevant friction coefficient and consequently the jamming volume fraction of the suspension. More precisely, the viscosity may be computed from the self-consistent relation:

$$\eta_S = \frac{\alpha\left(\mu(\Sigma)\right)}{\left(1 - \dfrac{\phi}{\phi_m\left(\mu\left(\Sigma\right)\right)}\right)^2} \tag{13}$$

where Σ is the normalized shear stress:

$$\Sigma = \frac{6\pi a_1^2 \sigma}{1.69\ L_c} = \frac{F_n}{L_c} \tag{14}$$

and the relevant friction coefficient is given by Eqn. (11), in the STIVF model. Note that a_1 is 0.8 times the mean radius, so in the following we will take $a_1 = 0.8\,a = 16\,\mu m$.

$\alpha(\mu)$ and $\phi_m(\mu)$ are deduced from numerical simulations performed for various constant values of μ and are given by[25]:

$$\alpha(\mu) = \alpha^\infty + (\alpha^0 - \alpha^\infty)\frac{exp\left(-X^\alpha\ atan(\mu)\right) - exp\left(-\pi X^\alpha/2\right)}{1 - exp\left(-\pi X^\alpha/2\right)}$$

$$\phi_m(\mu) = \phi_m^\infty + (\phi_m^0 - \phi_m^\infty)\frac{exp\left(-X^p\ atan(\mu)\right) - exp\left(-\pi X^p/2\right)}{1 - exp\left(-\pi X^p/2\right)} \tag{15}$$

with the fitting parameters displayed in Table 1 (first line). The striking feature here is that the relevant friction coefficient in Eqn. (13) is actually the microscopic friction coefficient used in the discrete simulations. Therefore the influence of any particular microscopic friction law on the suspension viscosity may be easily probed without the need of further discrete simulations.

Table 1 fitting parameters

	α^0	α^∞	X^α	ϕ_m^0	$\phi_{m\infty}$	X^p
STIVF model[25]	1	0.64	1.85	0.70	0.546	2.43
This study	1	0.64	1.85	0.65	0.55	2.43

Using Eqns. (13)-(15), together with the experimental friction law (Eqn. (12)) and the values in table 1 (second line), we compute the relative viscosity. As shown in table 1, the values of the rheological parameters from the *STIVF* model were taken from Lobry *et al.*[25], except for ϕ_m^0 and ϕ_m^∞ that we take here equal to 0.65 and 0.55 instead of 0.7 and 0.546, respectively.

The results are presented in Fig. 9 together with the experimental results. Note that the friction coefficient has been measured in the same ranges of force and contact velocity as those explored in the rheometric experiments. In rheometry, the interparticle force range is given by: $F = 6\pi a^2\sigma/1.69 \approx 10 - 1500\,nN$ and the relative velocity experienced by the particles by $v \approx a\dot{\gamma} \approx 10 - 1500\,\mu m/s$. In AFM experiments, normal force has been varied between $10\,nN$ (the estimated resolution) and $1\,\mu N$ and the relative velocity of particles ($v = 2\pi f y_0$) between 10 and $1200\,\mu m/s$.

The agreement between the experimental results obtained for five different volume fractions and the *STIVF* model[25] is excellent. This quantitative agreement shows that the rheology of concentrated non-Brownian suspensions is actually controlled by the frictional properties of the particles, as proposed by several authors[10,14,24]. It appears that the numerical simulations of Lobry *et al.* carried out with a constant friction coefficient have made it possible to propose reliable fitting laws for linking the viscosity to the friction coefficient. Moreover, the good agreement validates many of the hypotheses of the *STIVF* model and, in particular, the choice to describe the contact between particles by a Brizmer-type single-asperity contact model. The variation of the friction coefficient with normal load measured by AFM for normal forces of the same magnitude as those experienced by particles in sheared suspensions is qualitatively close to that predicted by the Brizmer model, which justifies the use of the latter to predict the shear-thinning of concentrated non-Brownian suspensions, as proposed in the *STIVF* model. Finally, the agreement between the experimental results and the model also highlights the interest and the relevance of the model in Eqn. (13-15), which establishes a direct connection between the suspension viscosity and the microscopic

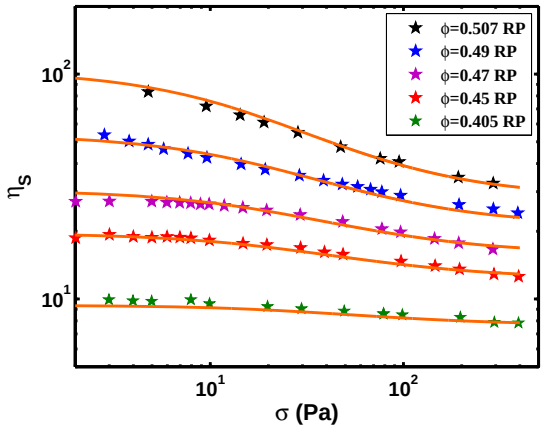

Fig. 9 Normalized viscosity versus shear stress. The symbols represent the experimental measurements performed with the suspensions of non-washed TS40 microparticles for different particle volume fractions while the orange lines are the results of the model with only two free parameters that are ϕ_m^0 and ϕ_m^∞, the jamming fractions of suspensions made of frictionless and infinitely frictional particles respectively. Note that only viscosity data obtained for stresses that correspond to the force range in which the friction coefficient has been measured are shown.

friction coefficient, by means of the relevant shear induced contact force $6\pi a^2\sigma/1.69$.

5 Conclusions

The comparison of the rheology of washed or raw particle suspensions – i.e. in the absence or presence of surfactant – allowed us first to distinguish the respective effects of adhesion and load-dependent friction properties on the shear-thinning of concentrated non-Brownian suspensions. This rapid comparison echoes the detailed study conducted by Papadopoulou *et al.* [22] on these respective roles and is not the essential result of our paper.

The core of our message is to confirm the scenario proposed by Lobry *et al.* in the *STIVF* model that variable friction between particles is at the origin of shear-thinning. To this purpose, we first carried out AFM measurements in order to determine the friction coefficient of the $TS40$ microspheres and its variation with the normal force in the force range experienced by particles in a sheared suspension. The friction coefficient has been shown to decrease with increasing load, which contrasts to the constant friction coefficient usually observed in the case of contacting macroscopic bodies. This behavior suggests that the contact between particles involves a small number of asperities, as proposed in the *STIVF* model. The measured friction law slightly differs from the law proposed by Brizmer *et al.* [32] to describe the friction that occurs between a single smooth hemisphere (the asperity) and a plane. The discrepancy may be explained by the geometry of the surface asperities which is certainly more complicated than the ideal hemisphere considered by Brizmer *et al.* Nevertheless the experimental friction law displays the same trends as the mono-asperity contact model: at small load, in the elastic deformation regime, the friction coefficient decreases, and it levels off as the normal force increases sufficiently for plastic deformation to occur. The characteristic force L_c that marks the transition from a fully elastic to a plastic contact has been found quite close to the value deduced from the roughness size and the mechanical properties (Young modulus and yield strength) of polystyrene.

Despite these slight differences, the correlation observed between the decrease in friction coefficient and the decrease in viscosity supports the scenario used in the *STIVF* model and highlights the close links between the microscopic friction properties of the particles and the macroscopic rheological behavior of the suspension. Furthermore, the quantitative agreement between the predictions of the rheological model where the experimental microscopic friction law has been introduced and the experimental measurements of the viscosity should be stressed. This makes the *STIVF* model an accurate tool able to quantitatively predict the rheology of moderately concentrated non-Brownian suspensions from the microscopic contact law.

To go further, it would be interesting to reproduce this study with other particles that could be made of a different material or have particular surface properties (electrically charged or grafted with polymer brushes). Finally, in the case of adhesive suspensions, it would be interesting to characterize the adhesion forces using an AFM and to jointly study the rheology of these suspensions in order to establish quantitative links between adhesion and rheology (yield stress, shear-thinning), as it has been done for friction.

Author contributions

Author contributions are defined based on the CRediT (Contributor Roles Taxonomy) and listed alphabetically. Conceptualization: EL, LL, FP. Formal analysis: EL, AM. Funding acquisition: EL. Investigation: MA, CC, EL. Methodology: EL, AM, FP, . Project administration: EL. Supervision: EL, AM. Writing original draft: EL. Writing review and editing: MA, CC, EL, LL, AM, FP.

Conflicts of interest

There are no conflicts to declare.

Acknowledgements

This work was supported by the French National Agency (ANR) under the program Blanc AMARHEO (ANR-18-CE06-0009-01). Muhammad Arshad acknowledges financial support from the Higher Education Commission of Pakistan.

Notes and references

1 É. Guazzelli and O. Pouliquen, *Journal of Fluid Mechanics*, 2018, **852**, year.
2 S. Jamali, E. Del Gado and J. F. Morris, *Journal of Rheology*, 2020, **64**, 1501–1524.
3 S. Gallier, E. Lemaire, F. Peters and L. Lobry, *Journal of Fluid Mechanics*, 2014, **757**, 514–549.
4 R. Mari, R. Seto, J. F. Morris and M. M. Denn, *Journal of Rheology*, 2014, **58**, 1693–1724.
5 F. Peters, G. Ghigliotti, S. Gallier, F. Blanc, E. Lemaire and L. Lobry, *Journal of rheology*, 2016, **60**, 715–732.
6 O. Cheal and C. Ness, *Journal of rheology*, 2018, **62**, 501–512.

7 W. Chèvremont, B. Chareyre and H. Bodiguel, *Physical Review Fluids*, 2019, **4**, 064302.

8 M. Wyart and M. Cates, *Physical review letters*, 2014, **112**, 098302.

9 J. Comtet, G. Chatté, A. Niguès, L. Bocquet, A. Siria and A. Colin, *Nature communications*, 2017, **8**, 1–7.

10 G. Chatté, J. Comtet, A. Niguès, L. Bocquet, A. Siria, G. Ducouret, F. Lequeux, N. Lenoir, G. Ovarlez and A. Colin, *Soft matter*, 2018, **14**, 879–893.

11 H. Perrin, C. Clavaud, M. Wyart, B. Metzger and Y. Forterre, *Physical Review X*, 2019, **9**, 031027.

12 R. Seto, R. Mari, J. F. Morris and M. M. Denn, *Physical review letters*, 2013, **111**, 218301.

13 B. Guy, M. Hermes and W. C. Poon, *Physical review letters*, 2015, **115**, 088304.

14 C. Clavaud, A. Bérut, B. Metzger and Y. Forterre, *Proceedings of the National Academy of Sciences*, 2017, **114**, 5147–5152.

15 C.-P. Hsu, S. N. Ramakrishna, M. Zanini, N. D. Spencer and L. Isa, *Proceedings of the National Academy of Sciences*, 2018, **115**, 5117–5122.

16 N. Fernandez, J. Cayer-Barrioz, L. Isa and N. D. Spencer, *Langmuir*, 2015, **31**, 8809–8817.

17 N. M. James, C.-P. Hsu, N. D. Spencer, H. M. Jaeger and L. Isa, *The journal of physical chemistry letters*, 2019, **10**, 1663–1668.

18 F. Gadala-Maria and A. Acrivos, *Journal of Rheology*, 1980, **24**, 799–814.

19 A. Vázquez-Quesada, R. I. Tanner and M. Ellero, *Physical review letters*, 2016, **117**, 108001.

20 A. Vázquez-Quesada, A. Mahmud, S. Dai, M. Ellero and R. I. Tanner, *Journal of Non-Newtonian Fluid Mechanics*, 2017, **248**, 1–7.

21 F. Blanc, E. d'Ambrosio, L. Lobry, F. Peters and E. Lemaire, *Physical Review Fluids*, 2018, **3**, 114303.

22 A. Papadopoulou, J. J. Gillissen, H. J. Wilson, M. K. Tiwari and S. Balabani, *Journal of Non-Newtonian Fluid Mechanics*, 2020, 104298.

23 J. A. Richards, B. M. Guy, E. Blanco, M. Hermes, G. Poy and W. C. Poon, *Journal of Rheology*, 2020, **64**, 405–412.

24 R. I. Tanner, C. Ness, A. Mahmud, S. Dai and J. Moon, *Rheologica Acta*, 2018, **57**, 635–643.

25 L. Lobry, E. Lemaire, F. Blanc, S. Gallier and F. Peters, *Journal of Fluid Mechanics*, 2019, **860**, 682–710.

26 P. Pham, B. Metzger and J. E. Butler, *Physics of Fluids*, 2015, **27**, 051701.

27 F. Blanc, F. Peters and E. Lemaire, *Physical review letters*, 2011, **107**, 208302.

28 J. Greenwood and D. Tabor, *Proceedings of the Physical Society*, 1958, **71**, 989.

29 C. Hoyle, S. Dai, R. Tanner and A. Jabbarzadeh, *Journal of Non-Newtonian Fluid Mechanics*, 2020, **276**, 104235.

30 R. I. Tanner, *Journal of Non-Newtonian Fluid Mechanics*, 2020, 104282.

31 R. V. More and A. M. Ardekani, *Journal of Rheology*, 2020, **64**, 67–80.

32 V. Brizmer, Y. Kligerman and I. Etsion, *Tribology Letters*, 2007, **25**, 61–70.

33 S.-C. Dai, E. Bertevas, F. Qi and R. I. Tanner, *Journal of Rheology*, 2013, **57**, 493–510.

34 A. K. Nyhus, A.-M. Johansen and S. Tøgersen, *Process for the production of particular polymers*, 2005, US Patent 6,875,799.

35 S. Gallier, E. Lemaire, L. Lobry and F. Peters, *Journal of Fluid Mechanics*, 2016, **799**, 100–127.

36 A. W. Chow, S. W. Sinton, J. H. Iwamiya and T. S. Stephens, *Physics of Fluids*, 1994, **6**, 2561–2576.

37 D. Merhi, E. Lemaire, G. Bossis and F. Moukalled, *Journal of Rheology*, 2005, **49**, 1429–1448.

38 K. L. Johnson, K. Kendall and a. Roberts, *Proceedings of the royal society of London. A. mathematical and physical sciences*, 1971, **324**, 301–313.

39 C. S. Hodges, J. A. Cleaver, M. Ghadiri, R. Jones and H. M. Pollock, *Langmuir*, 2002, **18**, 5741–5748.

40 S. Garland, G. Gauthier, J. Martin and J. Morris, *Journal of Rheology*, 2013, **57**, 71–88.

41 J. Y. Moon, S. Dai, L. Chang, J. S. Lee and R. I. Tanner, *Journal of Non-Newtonian Fluid Mechanics*, 2015, **223**, 233–239.

42 F.-J. Schmitt, T. Ederth, P. Weidenhammer, P. Claesson and H.-J. Jacobasch, *Journal of adhesion science and technology*, 1999, **13**, 79–96.

43 A. Faghihnejad and H. Zeng, *Soft Matter*, 2012, **8**, 2746–2759.

44 H. Barnes, *Journal of Rheology*, 1989, **33**, 329–366.

45 A. Singh, R. Mari, M. M. Denn and J. F. Morris, *Journal of Rheology*, 2018, **62**, 457–468.

46 A. Singh, S. Pednekar, J. Chun, M. M. Denn and J. F. Morris, *Physical review letters*, 2019, **122**, 098004.

47 J. Cleveland, S. Manne, D. Bocek and P. Hansma, *Review of scientific instruments*, 1993, **64**, 403–405.

48 J. E. Sader, *Journal of applied physics*, 1998, **84**, 64–76.

49 A. Weisenhorn, P. Hansma, T. Albrecht and C. Quate, *Applied physics letters*, 1989, **54**, 2651–2653.

50 V. S. Craig and C. Neto, *Langmuir*, 2001, **17**, 6018–6022.

51 A. Mongruel, T. Chastel, E. S. Asmolov and O. I. Vinogradova, *Physical Review E*, 2013, **87**, 011002.

52 S. Ryu and C. Franck, *Langmuir*, 2011, **27**, 13390–13399.

53 A. J. Goldman, R. G. Cox and H. Brenner, *Chemical engineering science*, 1967, **22**, 637–651.